HHS Public Access

Author manuscript

*Microvasc Res*. Author manuscript; available in PMC 2020 May 22.

Published in final edited form as:

*Microvasc Res*. 2018 March ; 116: 77–86. doi:10.1016/j.mvr.2017.09.003.

# Emergent behaviors in RBCs flows in micro-channels using digital particle image velocimetry

**Cairone F.**[a,*], **Ortiz D.**[b], **Cabrales P.J.**[b], **Intaglietta M.**[b], **Bucolo M.**[a]

[a]Department of Electrical, Electronic and Computer Science Engineering, University of Catania, Italy

[b]Department of Bioengineering, University of California San Diego, California, USA

## Abstract

The key points in the design of microfluidic Lab-On-a-Chips for blood tests are the simplicity of the microfluidic chip geometry, the portability of the monitoring system and the ease on-chip integration of the data analysis procedure. The majority of those, recently designed, have been used for blood separation, however their introduction, also, for pathological conditions diagnosis would be important in different biomedical contexts. To overcome this lack is necessary to establish the relation between the RBCs flow and blood viscosity changes in micro-vessels. For that, the development of methods to analyze the dynamics of the RBCs flows in networks of micro-channels becomes essential in the study of RBCs flows in micro-vascular networks. A simplification in the experimental set-up and in the approach for the data collection and analysis could contribute significantly to understand the relation between the blood non-Newtonian properties and the emergent behaviors in collective RBCs flows.

In this paper, we have investigated the collective behaviors of RBCs in a micro-channel in unsteady conditions, using a simplified monitoring set-up and implementing a 2D image processing procedure based on the digital particle image velocimetry. Our experimental study consisted in the analysis of RBCs motions freely in the micro-channel and driven by an external pressure. Despite the equipment minimal complexity, the advanced signal processing method implemented has allowed a significant qualitative and quantitative classification of the RBCs behaviors and the dynamical characterization of the particles velocities along both the horizontal and vertical directions. The concurrent causes for the particles displacement as the base solution-particles interaction, particle-particle interaction, and the external force due to pressure gradient were accounted in the results interpretation. The method implemented and the results obtained represent a proof of concept toward the realization of a general-purpose microfluidic LOC device for *in-vitro* flow analysis of RBCs collective behaviors.

## 1. Introduction

Microfluidic Lab-On-a-Chip (LOC) technology represents a revolution in laboratory experimentation, bringing the benefits of miniaturization, integration and, automation to

*Corresponding author. fcairone@dieei.unict.it (F. Cairone).

many research-based industries and biomedical applications (Janasek et al., 2006; Whitesides, 2006).

In the microvascular research, advances in microfluidic LOCs have resulted in the miniaturization of disposable devices for particles separation (Nivedita and Papautsky, 2013) and test for blood viscosity (Kang et al., 2013).

Red blood cells (RBCs) are the principal determinants its hemo-rheological properties (Popel and Johnson, 2005) of blood, particularly in the microvascular regions where they perform their essential functions and blood vessels diameters vary from 1 mm to a diameter smaller than that of the individual cells (~7 μm). RBCs are highly deformable (Tomaiuolo and Guido, 2011) and tend to aggregate (Tomaiuolo et al., 2016; Wagner et al., 2013). Those properties lead to the non-Newtonian blood behavior in micro-vessels (Fedosov et al., 2014; Pan et al., 2011) which affects the flow especially at microcirculation and is of great importance in the diagnosis of different pathological conditions (Campo-Deaño et al., 2013; Tomaiuolo, 2014).

Effects of the aggregation are the blunt velocity profile, related to the viscosity increase (Bishop et al., 2001), and the enhancement of the RBCs lateral migration. This cells displacement brings a low cellular density near the walls and the formation of “cell free layers” (CFLs), that can be associated with a viscosity decrease in those areas (Kim et al., 2009). Other parameters that can affect the CFL formation are: the hematocrit, the structure of the micro-vessel network and the flow rate (Kim et al., 2007; Yin et al., 2013). Different experimental results in the literature have shown that flow and viscosity changes in microvessels can be related to aggregation, leading to either its increase (Bishop et al., 2001) or decrease (Baskurt et al., 1999), however the functional relation between RBCs aggregation and RBCs flow is still under investigation.

Certainly, the aggregation depends on the RBCs collective behavior. For that, the development of methods to analyze the dynamics of the RBCs flows in networks of micro-channels (Campo-Deaño et al., 2013; Sherwood, 2012) is essential in the study of RBCs flows in micro-vascular networks.

A simplification in the experimental set-up and in the approach for the data collection and analysis could contribute significantly to understand the relation between the blood non-Newtonian properties and the emergent behaviors in collective RBCs flows. In this paper, we have investigated the collective behaviors of RBCs in a rectilinear microchannel in unsteady conditions, using a simplified monitoring set-up and implementing a 2D image processing procedure based on the digital particle image velocimetry (Raffel et al., 1998). Despite the minimal complexity of the equipment and of the analysis method defined, a significant qualitative and quantitative classification of the RBCs collective behaviors and a dynamical characterization of the particles velocities was obtained.

The development of reliable optical technique to measure the RBCs velocity and to characterize the flow dynamics has been raising the attention of research community (João and Gambaruto, 2014; Pinho et al., 2013) being slightly invasive and suitable for both small or large micro-channels and micro-vessels. Based on the experimental conditions both

images and signals based approaches have been widely used, as the Particle Image Velocimetry (PIV) or Particle Tracking (Sapuppo et al., 2008; Ha et al., 2012) and the Dual-Slit method (Sapuppo et al., 2007; Roman et al., 2012). However, in most cases, the monitoring systems are bulky or include highly complex optical set-up, and tend to be costly like for the μPIV (Van Steijn et al., 2007). These systems, although endowed with a high 3D precision, cannot be considered suitable for the on-chip integration (Sapuppo et al., 2010; Cairone et al., 2016).

The method presented in this paper to investigate the RBCs flows is at the same time optically based and focused on the key aspects for a future design of a microfluidics LOC: the simplicity of the microfluidic chip geometry; the portability of monitoring system and the easy on-chip integration of the data analysis. A simplification in the approach for the data collecting and analysis could widen significantly the research in this direction. A 2D image processing analysis based on the Digital Particle Image Velocimetry (DPIV) (Raffel et al., 1998) was performed to compute the velocities of the collective RBCs flow in the micro-channel. Although the simplification adopted in the optical setting and the algorithm, in the experimental campaigns realized the RBCs movements both in free and forced conditions were clearly characterized and quantified. It was possible to establish an association between the flow patterns identified and the velocity fields of the RBCs. The dynamical change of velocity field in time was correlated to the forcing input strength by a signals analysis procedure in the frequency domain and, the spatial distribution of the RBCs velocities was represented by maps. A flow dynamic interpretation was established considering the concurrent causes for the particles displacement: the base solution-particles interaction, the particle-particle interaction and the external pressure gradient. The nonlinear interplay between the cells and the flow generates complex dynamics still unexplored (Dupire et al., 2012). Those interactions could be justified in a general context by the Van der Waals forces, discussed in literature for both inorganic and biological systems (Kendall and Roberts, 2015), as well as, referred to the specific attractive force (binding force) among RBCs (Tomaiuolo, 2014), or to the RBC flicker (Burton et al., 1968) and the RBCs shape memory phenomenon (Fisher, 2004). A detailed study on the origin of the RBCs movements detected is far from this paper focus, that instead want to propose a method to be easily adopted for their investigation.

The paper is organized as follows. The Section 2 describes in details the experimental approach and the method implemented for data analysis. The Section 3 illustrates the results obtained and their correlation in the different experimental conditions.

## 2. Materials and methods

### 2.1. Experimental setup

A cycloolefin copolymer microfluidic rectilinear *Y*-junction (SMS0104, ThinxxS), with a squared area of 320 μm side and a length of 16 mm was used as shown in Fig. 1(a). One inlet was plugged and RBCs sample was fed at the second inlet. RBCs sample, as a two-phase fluid, was obtained by diluting fresh blood taken from a hamster to a concentration of 1% (hematocrit) in a phosphate buffered saline (PBS). The hematocrit level was set at 1% to allow a clear detection of the RBCs flow by 2D imaging. A peristaltic pump (Instech P625)

controlled by an *ad-hoc* LABVIEW interface, was used to feed the fluid-mix in the microfluidic channel.

Six experiments are presented. In the first (labelled as {*PBS*}), a single-phase PBS flow was forced at the inlet with an oscillating pressure with a frequency $f = 0.1$ Hz and an amplitude of $A = 100$ mm Hg (equivalent to 13.33 kPa). In the second experiment (labelled as $\{A = 0\}$), the channel was filled with the RBCs sample and connected with the pump in a switched-off mode. During the other four experiments the pump was switched-on and an external oscillating pressure at a frequency $f = 0.1$ Hz with an amplitude varying for each trial in the set $A \in \{0.1; 1; 10; 100\}$ mm Hg (equivalent to $A \in \{0.0133; 0.133; 1.33; 13.33\}$ kPa) was applied at the inlet, labelled respectively with the amplitude strength.

A backlit white light microscope (BX51, Olympus) with a magnification of 10× and coupled with an high-speed CCD (PCA 1024, Photron) was used as optical monitoring system. Generally, much of the PIV analysis is performed by using the laser, but also white light can be used (Raffel et al., 1998; Poelma et al., 2012). The light sources such as the halogen lamps are well suited in connection with CCD camera for its spectral sensitivity. Other advantages are the low cost, the simplicity and no needs of particles tracer. Based on the microscope set-up (Olympus BX51, and working distance of the objective 3.5 mm), the focal plane was placed, with a good approximation, at the center of the microchannel. The correct position was achieved thanks to the autofocus unit embedded in the microscope system (Olympus BX51) that maintains the wanted position.

The video circumscribed an area of 1 $mm^2$ with the micro-channel at the center and at a distance of 8 mm from the inlet. It was recorded for about 12 s with a sample rate of 125 Hz. A view of the opto-microfluidic set-up is shown in Fig. 1(b) with a zoom of the microfluidic chip position under the microscope.

The single-phase {*PBS*} solution was analyzed to quantify of the background movements, due to the presence of the PBS itself, selected as the RBCs flow medium. The RBCs flow was detected in all five movies acquired, and $A \in \{0; 0.1; 1; 10; 100\}$, including when the pump was inactive. To evidence the particle distribution in the micro-channel, one frame per experiment is shown in Fig. 1(c). For $A \in \{0; 10; 100\}$ there is a uniform distribution of RBCs in the whole micro-channel, whereas for $A \in \{0.1; 1\}$ the RBCs are grouped in specific areas. These spatial distributions were maintained during all the experiments. For each experimental condition the mean of the RBCs adhesion at a distance of 40 μm from both walls has been computed in percentage respect to the total number of particles in the ROI, obtaining respectively for the experiments $A \in \{0; 0.1; 1; 10; 100\}$ the values {31.8%; 31.5%; 32,2%; 27,1%; 25,3%}. After the experiment $\{A = 1\}$ the increase of the forcing input led to a decrease of adhesion.

## 2.2. DPIV analysis

The RBCs flow movies were analyzed using the Digital Particle Image Velocimetry (DPIV) (Raffel et al., 1998) and time-varying velocities vector maps showing the RBCs displacements were obtained (see Fig. 2). Those velocities maps are then considered to

investigate the RBCs flow patterns and to correlate the dynamics of the flow velocity in the time and frequency with the experimental conditions $A \in \{0, 0.1; 1; 10; 100\}$.

The videos acquired consisted in sequences of around 1800 frames of size (1024 × 1024 px) with a spatial resolution of 1 pixel = 1 μm, where RBCs flow occupies only a portion of that area, called region of interest (ROI). The height of the ROI considered was 300 μm being the real micro-channel height 320 μm and 10 μm from each wall strongly affected by the phenomena of the light refraction (see Fig. 1(c)). The ROI position inside the image was set by the left-top corner of the micro-channel as the starting pixel ($x_0 = 1$, $y_0 = 400$) and the desired width and the height respectively at $x_{ROI} = 1024$ px and $y_{ROI} = 300$ px (see Figs. 1(c) and 2).

The DPIV analysis implements the cross-correlation between the interrogations areas of consecutive pair of images as the most probable displacement of the particle inside the area considered. The approach used for the image correlation analysis was the discrete Fourier transform (DFT) in frequency domain where the Fourier transform is applied to the interrogation areas of both images; then the product, in the complex domain, of these transforms is computed and anti-transformed, using the inverse FFT (Thielicke and Stamhuis, 2014). From one hand, the DFT requires a smaller computational effort than the other method available (Raffel et al., 1998) but, from the other hand, having a fixed dimension for the interrogation areas a loss of information related to the displacement of particles could be determined. To overcome this accuracy decrease, the multi-pass DFT can be used choosing a bigger interrogation area in the first pass, and smaller areas in the successive steps.

In this work, a three-pass DFT was set by using the platform JPIV (Java Particle Image Velocimetry) (http://www.jpiv.vennemannonline.de/). The step size has been chosen to be a half of the last interrogation area and the subsequent interrogation areas half that in the previous step as follows: *InterrArea* 1 = 64, *InterrArea* 2 = 32, *InterrArea* 3 = 16 and the *Step* = 8. In this way, the smallest displacement investigated is of about 8μm, close to the double of particle dimension.

The DPIV analysis was performed on all the six movies, obtaining a time varying velocity vector $V_{x,y}(t)$ associated with two spatial components ($x$, $y$) for each point of the map. The two velocity components ($V_x(t)$, $V_y(t)$), were computed as the projections of the velocity vector along the horizontal ($x$) and vertical ($y$) directions (see Fig. 1(c)). At a time instant ($t$), the results visualization was possible by the velocity vectors maps $V(t)$, in which arrows display the RBCs velocity in module (coded by the color and the vector length) and direction (coded by the vector orientation) (see Fig. 2). The size of the velocity map depends on selected ROI size (1024 × 300 px), on the values of the interrogation areas and on the quantization step, according to the set of Eq. (1):

$$maxJ = step * floor\left(\frac{J_{ROI}}{step}\right) - (InterrArea - 1) + \frac{InterrArea}{2}$$
$$minJ = 1 + \frac{InterrArea}{2} \quad (1)$$
$$dimJ = floor\left(\frac{maxJ - minJ}{step} + 1\right)$$

where *dim_J* is assumed as the map dimension (either on the *x* or *y* direction) and $J_{ROI}$ the respective ROI dimension. Based on the DPIV setting used, the size of velocity map was (121 × 33 px) with a spatial resolution of about 8 μm. The velocity is given in [mm/s].

## 3. Results

Initially the time-varying vectors maps were classified by visual inspection and three different flow patterns were identified. Then the two time-varying velocity components along the horizontal and vertical direction ($V_x(t)$, $V_y(t)$) for each vector map position (*x*, *y*) were computed and then spatially and temporally averaged. The spatial average produced two signals ($\langle V_x(t)\rangle$, $\langle V_y(t)\rangle$) representative of the mean RBCs velocities, respectively on *x* and *y* directions *versus* time. The dynamics of both signals were analyzed in time and in frequency domain. The temporal average generated two maps ($\langle V_x\rangle$, $\langle V_y\rangle$) that reconstruct for each point of the area (*x*, *y*) under investigation the mean of the RBCs velocities assumed respectively on the *x* and *y* directions. In the following sub-sections the results are discussed, describing how the flow patterns identified and the dynamics of the velocities components can be correlated with the different experimental conditions.

### 3.1. RBCs flow patterns

By the investigation of the time-varying velocity vector fields, it was possible to identify three different behavioral patterns (see Fig. 3) and classified as *Weak Activity*, *Vorticity*, and *Alignment*. Moving from one pattern to the subsequent it can be to notice an increase of the RBCs mean velocity and a vector re-orientation. The velocity increase can be correlated to the number of moving RBCs (number of the arrows) and their velocities (color and length of the arrows). The *Weak Activity* was associated with a powerless and localized random stream. The vector re-orientation consisted of RBCs displacements in vortex randomly distributed along the channel length followed, defined as *Vorticity*, by an ordered arrangement of their displacements along the horizontal direction, defined as *Alignment*.

Starting from those distinctions, the relation between the RBCs flow patterns and the RBCs velocities along the horizontal ($|\langle V_x(t)\rangle|$) and vertical ($|\langle V_y(t)\rangle|$) directions was established by the map shown in Fig. 4(a). This map was obtained by the data interpolation of 150 cases randomly selected from all the experiments and assuming the coding: “0” for the *Weak Activity*, “0.5” for the *Vorticity* and “1” for the *Alignment*. The *x*-axis and the *y*-axis report respectively the $|\langle V_y(t)\rangle|$ and the $|\langle V_x(t)\rangle|$ values in [mm/s], whereas the color codes the behaviors. The correlation between the RBCs behavioral areas and the ($|\langle V_y(t)\rangle|$, $|\langle V_x(t)\rangle|$) pairs follows:

- Weak Activity

Area–$w1$ $|<V_y(t)>| < 0.04$ and $0.0 < |<V_x(t)>| < 0.1$

- Vorticity

Area–$v1$ $|<V_y(t)>| < 0.04$ and $0.1 < |<V_x(t)>| < 0.2$

Area–$v2$ $|<V_y(t)>| < 0.02$ and $|<V_x(t)>| < 0.45$

Area–$v3$ $|<V_y(t)>| < 0.04$

- Alignment

Area–$a1$ $|<V_y(t)>| < 0.04$ and $0.2 < |<V_x(t)>| < 0.45$

Area–$a2$ $|<V_y(t)>| < 0.02$ *and* $|<V_x(t)>| > 0.45$

To investigate the RBCs flow behaviors possibly to be detected in the five experiments $A \in \{0; 0.1, 1\ 10; 100\}$ two statistical parameters were computed for both the velocity signals ($\langle V_x(t)\rangle$, $\langle V_y(t)\rangle$): the range of variation (as range ($\langle V_x(t)\rangle$) = $|max\langle V_x(t)\rangle|+|min\langle V_y(t)\rangle|$) and the standard deviation. These values are summarized in Table 1 and plotted in the histograms of Fig. 5. The statistics on $\langle V_y(t)\rangle$ are one order smaller than those of $\langle V_x(t)\rangle$ but their relative variations are similar. In the {*PBS*} experiment, the velocity obtained does not represent the actual {*PBS*} flow velocity but was used as reference value of the image processing method respect to the cases in which the RBCs displacements were detected. The statistics on the {*PBS*}, where no movement is expected, are used as control parameter. A greater range and variability were detected for $\langle V_x(t)\rangle$ in the experiments $A \in \{0; 10; 100\}$ and for $\langle V_y(t)\rangle$ in $A \in \{10; 100\}$.

To check the accuracy of the DPIV algorithm, the RBCs velocity was computed using the analytical solution proposed in (Bruus, 2008), for a Poiseuille PBS flow with a constant pressure (ΔP) at the inlet and a viscosity h = 1 *mPa s*. Having in our experiments an oscillating pressure at the inlet and a multi-phase fluid (RBC diluted at 1% in PBS), this approximation can be only partially valid. Assuming the lowest pressure (ΔP = 0.0133 *kPa*), the expected velocity was around 3 *mm*/*s*, one order greater than the maximum velocity obtained by DPIV analysis for the corresponding experiment {$A$ = *0.1*} 0.216 *mm*/*s*.

As expected from the statistics the *Alignment* was reached for $A \in \{0; 0{,}1; 10; 100\}$ whereas the experiment {$A$ = 1} reached the *Vorticity*. The *Alignment* is strongly correlated with higher $\langle V_x(t)\rangle$ values because the velocity vectors alignment implies a greater net flow compared with a randomly organization as in the *Vorticity*. The behavioral areas {Area-$v2$ and Area-$a2$} were detected only in the experiment {$A$ = 100}. As examples, to match the map with the experiments, the scattering plot related to ($|\langle V_y(t)\rangle|$, $|\langle V_x(t)\rangle|$) for $A \in \{0; 0.1; 10\}$ are shown in Fig. 4(b) highlighting the behavioral areas {Area-$w1$; Area-$v1$ Area-$a1$ and Area-$v3$}.

### 3.2. RBCs velocity dynamics in time domain

In Fig. 6 the velocity signals ($\langle V_x(t)\rangle$, $\langle V_y(t)\rangle$) of the five experiments $A \in \{0; 0.1; 1; 10; 100\}$ are plotted using a color-coded representation *versus* time. A zoom in a time window of 1 s is shown, selected after 4.8 s from the beginning of the experiments. The amplitude of

the signals ($\langle V_x(t)\rangle$, $\langle V_y(t)\rangle$) was normalized in the range [−1, 1] to enhance in the comparison in terms of flow dynamical changes. In Fig. 6(a) the horizontal displacements ($\langle V_x(t)\rangle$) of the particles in the micro-channel toward the left direction are associated to positive values (see Fig. 1(a) red arrow) whereas the right direction to negative values (see Fig. 1(a) blue arrow). In Fig. 6(b) the vertical displacements ($\langle V_y(t)\rangle$) are correlated to movement toward the wall_2 for positive velocities and toward the wall_1 for negative velocities (see Fig. 1(a)). In Fig. 6(a) the trends of $\langle V_x(t)\rangle$ for the experiments $A \in \{0; 0.1; 1\}$ shows a sequence of four periods lasting around 0.2 s. In each period, it is possible to distinguish two phases: a weak-activity ($|\langle V_x\rangle| \leq 0.5$ color-coded from green to orange) and a strong-activity ($0.5 \langle |\langle V_x\rangle| \langle 1$ color-coded in blue and red). The sequence of blue-red strips inside each period evidences the right-left oscillations of the RBCs displacement. The periodicity at 0.2 s can be detected also for $\{A = 100\}$ but all in the strong-activity range, moving from green-yellow ($|\langle V_x\rangle| \leq 0.2$) to the orange-red ($|\langle V_x\rangle| \geq 0.4$). In the Fig. 6(b) the trends of $\langle V_y\rangle$ for the five experiments $A \in \{0; 0.1; 1; 10; 100\}$ are compared and no periods can be detected by visual inspection. For the pressure strength $\{A = 100\}$ the activity on *y*-direction increases drastically.

A stronger activity is visible for both $\{A = 0\}$, where no forcing input is feeding the process and the particles displacement is due to spontaneous forces, and for $A \in \{10; 100\}$ when the control of the external pressure is the greater. This activity decreases for the input pressure $A \in \{0.1; 1\}$ can be caused by the contrast between the spontaneous forces driving the RBCs and input external force, resulting in weaker dynamics. In all conditions, the standard deviation is almost one order lower than the signal range confirming that the process randomness cannot be related with RBCs flow detected.

To highlight the effects of the peristaltic pump and the spontaneous dynamics emerging from the particles collective behaviors the trends of velocity along the horizontal axis $\langle V_x(t)\rangle$ for the experiments $A \in \{0.1; 10; 100\}$ in a time interval of 10s are reported in Fig. 7. The red line reproduces the trend of the periodic pressure wave at $f = 0.1$ Hz detected for $A \in \{10; 100\}$. It is worth to notice the process nonlinearity that emerges from the combined effect of the RBCs spontaneous and forced dynamics.

### 3.3. RBCs velocity dynamics in frequency domain

To widely investigate the period of oscillation observed in Figs. 6 and 7 the analysis of the signals ($\langle V_x(t)\rangle$, $\langle V_y(t)\rangle$) was performed in the frequency domain. Based on the acquisition conditions (frame rate and number of frames) the frequency domain investigated was $f \in [0.083; 62]$ Hz with a frequency step of 0.083 Hz. The artifact due to the power supply at 60 Hz was removed.

The component at $f = 0.1$ Hz directly induced by the pump pressure is detectable in the spectra of the experiments $\{PBS\}$ and $A \in \{10;100\}$. Being the change in the flow dynamics of the experiments $A \in \{0.1;1\}$ respect to $\{A = 0\}$ evident, presumably the effects of the external pressure is not enough strong to drive the process but acts as a perturbing disturbance (Bucolo et al., 2002).

Among all the frequencies components two peaks $f \in \{5; 17.5\}$ Hz have been selected as the most significant being highly sensitive to the experimental conditions and at the same time dominant at least in one experiment. A continuous counterbalance of these two frequency seems always present and dominant in the particles dynamics, whereas for the other peaks at $f \in \{12,5; 22.5\}$ Hz were not possible to establish a direct correlation with the experimental conditions. Assuming the nonlinearity of the process and based on concept of amplitude modulation (Papoulis and Pillai, 2001) widely known in the signal theory it seems to be feasible that they are originated from a linear combination of $f \in \{5; 17.5\}$ Hz, as their sum ($f = 17.5 + 5 = 22.5$ Hz) and difference ($f = 17.5–5 = 12.5$ Hz).

In Fig. 8(a) for all the six experimental conditions the spectra of the $\langle V_x(t) \rangle$ normalized by the number of frames are plotted. Particularly the $\{PBS\}$ experiment shows a broadband spectrum everywhere with a stronger activity around $f = 5$ Hz. The component at $f = 5$ Hz is dominant also in the spectrum of $\{A = 100\}$ whereas $f = 17.5$ Hz is dominant in all the other conditions $A \in \{0; 0.1; 1; 10\}$. A zoom of the spectra in the range $f \in [0.08; 10]$ Hz is reported in Fig. 8(b) to evidence the contribution of the peak $f = 5$ Hz in the experimental conditions $A \in \{0; 0.1; 1; 10\}$.

Being both frequencies $f \in \{5; 17.5\}$ Hz present in the experiment $\{A = 0\}$, when the pump switched-off, they could be correlated to the PBS-particles interaction or the particle-particle interaction in the micro-channel (Kendall and Roberts, 2015).

The peak at $f = 5$ Hz is also present in the spectra of $\langle V_y(t) \rangle$ together with an activity at high frequency $f = 55$ Hz affecting strongly the process for the pressure amplitude $A \in \{0.1; 1; 10\}$. As in the $\langle V_x(t) \rangle$, the greater contribution in the spectra of $\langle V_y(t) \rangle$ for $\{A = 100\}$ is for $f = 5$ Hz. The frequency component at $f = 5$ Hz is the only present in both spectra of ($\langle V_x(t) \rangle$, $\langle V_y(t) \rangle$) of all the experiments and in the $\langle V_x(t) \rangle$ spectrum of the $\{PBS\}$ flow, that enforces the hypothesis of a relation with the PBS-particles interaction induced by the physical and chemical properties of the PBS itself.

The histograms of the peaks amplitude at $f \in \{5; 17.5\}$ Hz in $\langle V_x(t) \rangle$ and at $f \in \{5; 55\}$ Hz in $\langle V_y(t) \rangle$ per experiment are reported respectively in Figs. 9 and 10. The histograms underline the amplitude modulation of these two peaks due to the forcing input. In Fig. 9(a)–(b) for both peaks at $f \in \{5; 17.5\}$ Hz, the initial value assumed for $\{A = 0\}$ is reduced when the pump is switched-on for $\{A = 0.1\}$. In Fig. 9(a) the peak at $f = 5$ Hz increases for $A \in \{0.1; 1; 10; 100\}$. In Fig. 9(b) the peak at $f = 17.5$ Hz increases with the forcing input amplitude for $A \in \{0.1; 1; 10\}$ and sharply decreases for $\{A = 100\}$.

The peak at $f = 5$ Hz in the spectra of $\langle V_y(t) \rangle$ follows the same amplitude modulation than in $\langle V_x(t) \rangle$, in a different scale (see Fig. 10(a)). The modulation of the activity at $f = 55$ Hz is plotted in Fig. 10(b), it increases $A \in \{0; 0.1; 1; 10; 100\}$ and sharply decreases for $\{A = 100\}$.

For a visual interpretation of the role played in the process by the frequency components identified $f \in \{5; 17.5\}$ Hz and associated respectively with the time periods $T \in \{0.2, 0.06\}$s, the signal $\langle V_x(t) \rangle$ was analyzed considering the right-left oscillations (see Fig. 6). The $\langle V_x(t) \rangle$ trend has been decomposed obtaining two signals to represent the dynamics of

the RBCs velocity in the left $\langle V_{xL}(t)\rangle$ and right $\langle V_{xR}(t)\rangle$ directions split. In both temporal evolutions are present the slow (T = 0.2 s) and the fast dynamics ($T$ = 0.06 s).

In Fig. 11, the signals ($\langle V_{xL}(t)\rangle$, $\langle V_{xR}(t)\rangle$) for the experiments $A \in \{0; 0.1;1; 10\}$ are shown respectively in red and blue line in a time window including two periods of 0.2 s. In Fig. 11(a)–(b)–(c) for $A \in \{0; 0.1; 1\}$ it can be observed that the particles displacements, in both direction ($\langle V_{xL}\rangle$, $\langle V_{xR}\rangle$) have the same intensity, and following a parabolic-like trend lasting 0.2 s, corresponding to frequency component at 5 Hz. The velocity increase is more regular in the right direction than in the left. Both the left and right oscillations are modulated by the fast component at 17.5 Hz ($T$ = 0.06 s). In Fig. 11(b)–(c) for $A \in \{0.1; 1\}$, when the pump is switched-on the amplitude of flow velocity in both direction ($\langle V_{xL}\rangle$, $\langle V_{xR}\rangle$) decreases respect to $\{A = 0\}$. In $\{A = 0.1\}$ the fast dynamics at $f$ = 17.5 Hz, coherently with the spectral analysis, is the smallest. The fast dynamic becomes dominant for $\{A = 10\}$ almost hiding the slow frequency (see Fig. 11(d)). This behavior is enhanced for {A = 100} where a broadband spectrum at high frequency and the strong modulation effect of the forcing pressure at 0.1 Hz do not allow to perceive by visual inspection the component at $f$ = 5 Hz.

### 3.4. RBCs spatial velocity distributions

The maps ($\langle V_x\rangle$; $\langle V_y\rangle$) of the particles velocity in each position of the micro-channel area were obtained by the temporal average of the velocity matrices ($V_x(t)$ and $V_y(t)$). Their absolute values ($|\langle V_x\rangle|$; $|\langle V_y\rangle|$) for the experiments $A \in \{0, 0.1; 1; 10; 100\}$ are shown respectively in Fig. 12(a)–(b). Each image was plotted using a color-coded threshold to have a comparison among experiments with $|\langle V_x\rangle| \leq 1$ and $|\langle V_y\rangle| \leq 0.5$. The thresholds were set at different values being the velocity on the vertical direction slower than in the horizontal. In Fig. 12(a)–(b) the red is for the greater velocity values ($|\langle V_x\rangle| > 0.5$ and $|\langle V_y\rangle| > 0.25$), and the blue for the smaller ($|\langle V_x\rangle| < 0.5$ and $|\langle V_y\rangle| < 0.25$). This representation allows to detect the areas in which the RBCs move faster.

In both Fig. 12(a)–(b), the spatial velocity maps of $|\langle V_x\rangle|$ and $|\langle V_y\rangle|$ show a higher RBCs velocity and particle density at the center of the micro-channel, and a slow flow at lower RBCs density in the areas near the walls for all the experimental conditions when the pump is active $A \in \{0.1; 1; 10; 100\}$.

This behavior becomes predominant increasing the amplitude ($A$) of the external force. That leads to correlate this distribution to a parabolic velocity profile, but with the discontinuity related to a non-uniform distribution of the particles along the channel. Particularly for $A \in \{0.1; 1\}$ where the formation of cells groups is clearly visible. This effect is lost when the RBCs activity increases due to a stronger external pressure.

It is worth to observe that different velocity distribution maps were identified when the pump is switched-off $\{A = 0\}$ and switched-on even at the lower input amplitude strength $\{A = 0.1\}$ (see Fig. 12). That can evidence a difference in the forces driving the processes. For $\{A = 0\}$ the faster movements can be detected close to the microchannel walls in $|\langle V_x\rangle|$, where the particles are located very close to each other in a higher concentration, and randomly distributed in $|\langle V_y\rangle|$. As expected, for $A \in \{0.1, 1, 10, 100\}$ the faster movements are always in the bulk flow in both maps ($|\langle V_x\rangle|$, $|\langle V_y\rangle|$).

## 4. Conclusions

In this paper, we have investigated the collective behaviors of RBCs in a micro-channel in unsteady conditions, using a simplified monitoring set-up and implementing a 2D image processing procedure based on the digital particle image velocimetry. Our experimental study consisted in the analysis of RBCs motions freely in the micro-channel and driven by an external pressure. Despite the equipment minimal complexity, the advanced signal processing method implemented has allowed a significant qualitative and quantitative classification of the RBCs behaviors and the dynamical characterization of the particles velocities along both the horizontal and vertical directions. The concept of collective behavior was introduced to study the RBCs flow in a group of cells, but not in a dense concentration, as in the condition of high hematocrit level, to highlight how the individual cell behavior can be affected by the surrounding cells but avoiding their dominance.

Three behavioral flow patterns {*Weak Activity*, *Vorticity* and *Alignment*} were identified by the time-varying vectors maps, then the signals related to the mean velocity on the horizontal and vertical direction ($\langle V_x(t)\rangle$, $\langle V_y(t)\rangle$) were used to successfully map the flow behaviors in all the experimental conditions.

The dynamical changes of both the velocity signals ($\langle V_x(t)\rangle$, $\langle V_y(t)\rangle$) were analyzed in time and in frequency domains. Two frequency components $f \in \{5; 17.5\}$ Hz have been selected as the most significant and it was possible to establish a direct correlation with the experimental conditions. Being both present in the dynamic of the experiment $\{A = 0\}$, where the pump is switched-off, they have been correlated to the PBS-particles interaction or the particle-particle interaction in the micro-channel. Particularly the presence in the spectrum of the *PBS* flow of the peak at $f = 5$ Hz suggests a relation with the physical and chemical properties of base-solution.

Despite similar behaviors in the RBCs flow patterns, it is significant to notice the difference in the velocity distributions obtained when the pump was inactive compared with those when the pump was switched-on. That underlines the difference in the forces driving the process in the two contexts, to be widely investigate in the future developments.

The results obtained open the way for different analysis. Within the limit imposed by the 2D image processing procedure, in a new experimental campaign it can be considered the effects induced by different hematocrit levels and the base solutions.

The flow features extracted and the simplification in the approach used for data collecting and analysis can be considered as a proof of concept on the validity of the proposed method aimed to correlate the blood flows and rheological properties. At the same time, the results confirm the chance to expand this method in a future development as a tool for cells differentiations and for a deeper investigation on the origin of the forces driving biological emergent behaviors.

Moreover, a further development of the algorithms and, a simplification and miniaturization in the set-up seem to be promising for future chip integration.

## References


Baskurt O, et al., 1999 The effect of red blood cell aggregation on blood flow resistance. Biorheology 36, 447–452. [PubMed: 10818644]

Bishop J, et al., 2001 Effect of erythrocyte aggregation on velocity profiles in venules. Am. J. Physiol. Heart Circ. Physiol. 280, H222–H236. [PubMed: 11123237]

Bruus H, 2008 Theoretical Microfluidics. Oxford University Press, New York.

Bucolo M, et al., 2002 Does chaos work better than noise. IEEE Circuits Syst. Mag. 2 (3), 4–19.

Burton AL, et al., 1968 Brief report: quantitative studies on the flicker phenomenon in the erythrocytes. Blood 32, 5.

Cairone F, et al., 2016 Micro-optofluidic switch realized by 3D printing technology. Microfluid. Nanofluid. 20, 61–71.

Campo-Deaño L, et al., 2013 Viscoelasticity of blood and viscoelastic blood analogues for use in polydimethylsiloxane in vitro models of circulatory system. Biomicrofluidics 7, 034102.

Dupire J, et al., 2012 Full dynamics of a red blood cell in shear flow. PNAS 109 (51), 20808–20813. [PubMed: 23213229]

Fedosov DA, et al., 2014 Multiscale modeling of blood flow: from single cells to blood rheology. Biomech. Model. Mechanobiol. 13, 239–258. [PubMed: 23670555]

Fisher TM, 2004 Shape memory of human red blood cells. Biophys. J. 86 (5), 3304–3313. [PubMed: 15111443]

Ha H, et al., 2012 Hybrid PIV–PTV technique for measuring blood flow in rat mesenteric vessels. Microvasc. Res. 84, 242–248. [PubMed: 22820216]

Janasek J, et al., 2006 Scaling the design of miniaturized chemical-analysis system. Nature 42, 374–380.

João A, Gambaruto A, 2014 Image Processing in the Tracking and Analysis of Red Blood Cell Motion in Micro-circulation Experiments. Visualization and Simulation of Complex Flows in Biomedical Engineering. Volume 12 of the series Lecture Notes in Computational Vision and Biomechanics pp. 133–149.

Kang YJ, et al., 2013 A microfluidic device for simultaneous measurement of viscosity and flow rate of blood in a complex fluidic network. Biomicrofluidics 7, 054111.

Kendall K, Roberts AD, 2015 van der Waals forces influencing adhesion of cells. Philos. Trans. R. Soc. B 370, 20140078.

Kim S, et al., 2007 Temporal and spatial variations of cell-free layer width in arterioles. Am. J. Physiol. Heart Circ. Physiol. 293, H1526–H1535. [PubMed: 17526647]

Kim S, et al., 2009 The cell-free layer in microvascular blood flow. Biorheology 46, 181–189. [PubMed: 19581726]

Nivedita N, Papautsky I, 2013 Continuous separation of blood cells in spiral microfluidic devices. Biomicrofluidics 7, 054101.

Pan W, et al., 2011 Predicting dynamics and rheology of blood flow: a comparative study of multiscale and low-dimensional models of red blood cells. Microvasc. Res. 82, 163–170. [PubMed: 21640731]

Papoulis A, Pillai SU, 2001 Probability, Random Variables and Stochastic Processes With Errata Sheet. McGraw-Hill Series in Electrical and Computer Engineering.

Pinho D, et al., 2013 Tracking Red Blood Cells in Microchannels: A Comparative Study Between an Automatic and a Manual Method. Topics in Medical Image Processing and Computational Vision. Volume 8 of the series Lecture Notes in Computational Vision and Biomechanics pp. 165–180.

Poelma C, et al., 2012 Accurate blood flow measurements: are artificial tracers necessary? PLoS ONE 2 (7(9)), e45247.

Popel AS, Johnson PC, 2005 Microcirculation and hemorheology. Annu. Rev. Fluid Mech. 37, 43–69. [PubMed: 21151769]

Raffel M, et al., 1998 Particle Image Velocimetry: A Practical Guide. Springer.

Roman S, et al., 2012 Velocimetry of red blood cells in microvessels by the dual-slit method: effect of velocity gradients. Microvasc. Res. 84, 249–261. [PubMed: 22963788]

Sapuppo F, et al., 2007 An improved instrument for real-time measurement of blood velocity in microvessels. Trans. Inst. Meas. 56 (6), 2663–2671.

Sapuppo F, et al., 2008 Microfluidics real-time monitoring using CNN technology. Trans. Biomed. Circuits Syst. 2 (2), 78–87.

Sapuppo F, et al., 2010 A polymeric micro-optical interface for flow monitoring in biomicrofluidics. Biomicrofluidics 4 (1), 1–13.

Sherwood JM, 2012 The effect of red blood cell aggregation on velocity and cell-depleted layer characteristics of blood in a bifurcating microchannel. Biomicrofluidics 6, 024119 (2012).

Thielicke W, Stamhuis EJ, 2014 PIVlab – towards user-friendly, affordable and accurate digital particle image velocimetry in MATLAB. J. Open Res. Softw. 2, e30.

Tomaiuolo G, 2014 Biomechanical properties of red blood cells in health and disease toward microfluidics. Biomicrofluidics 8, 051501. [PubMed: 25332724]

Tomaiuolo G, Guido S, 2011 Start-up shape dynamics of red blood cells in microcapillary flow. Microvasc. Res. 82, 35–41. [PubMed: 21397612]

Tomaiuolo G, et al., 2016 Microconfined flow behavior of red blood cells. Med. Eng. Phys. 38, 11–16. [PubMed: 26071649]

Van Steijn V, et al., 2007 PIV study of the formation of the segmented flow in microfluidic T-junction. Chem. Eng. Sci. 62, 7505–7514.

Wagner C, et al., 2013 Aggregation of red blood cells: from rouleaux to clot formation. C. R. Phys. 14, 459–469.

Whitesides GM, 2006 The origin and the future of microfluidics. Nature 42, 368–373.

Yin X, et al., 2013 Multiple red blood cell flows through microvascular bifurcations: cell free layer, cell trajectory, and hematocrit separation. Microvasc. Res. 89, 47–56. [PubMed: 23727384]

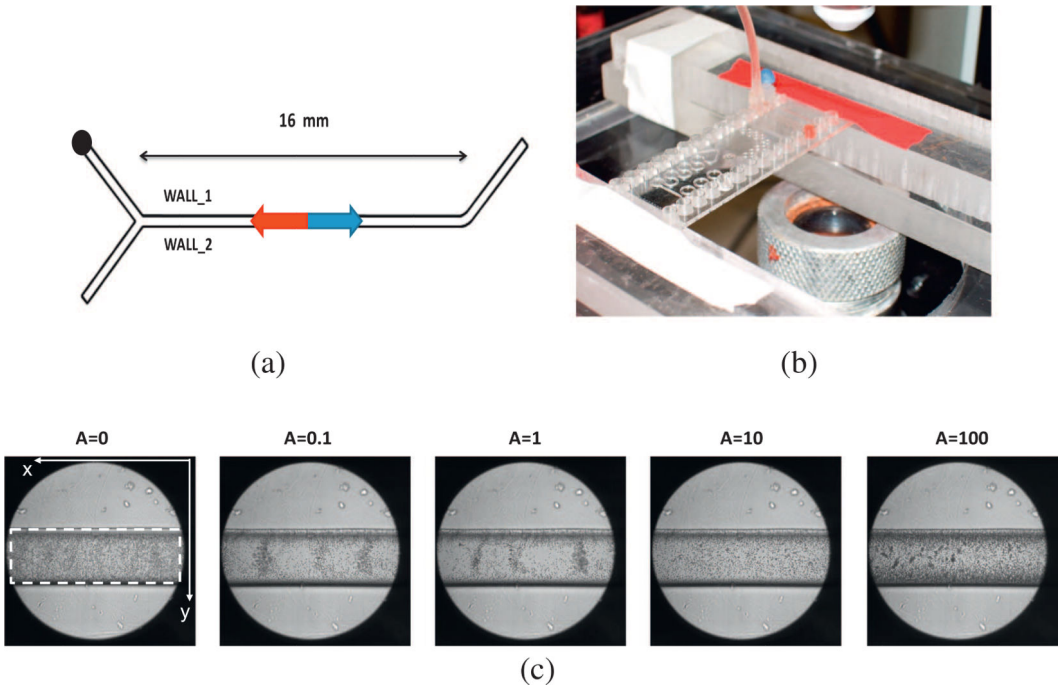


**Fig. 1.**

(a) The Y-junction geometry, the rectilinear microfluidic channel width $w = 320$ μm and length $l = 16$ mm. (b) The zoom of the microfluidic chip positioned under the microscope. (c) Five frames showing the RBCs sample distribution per experiment: a uniform distribution in the experiments with $A \in \{0, 10, 100\}$; the RBCs grouped in specific zones with $A \in \{0.1, 1\}$.

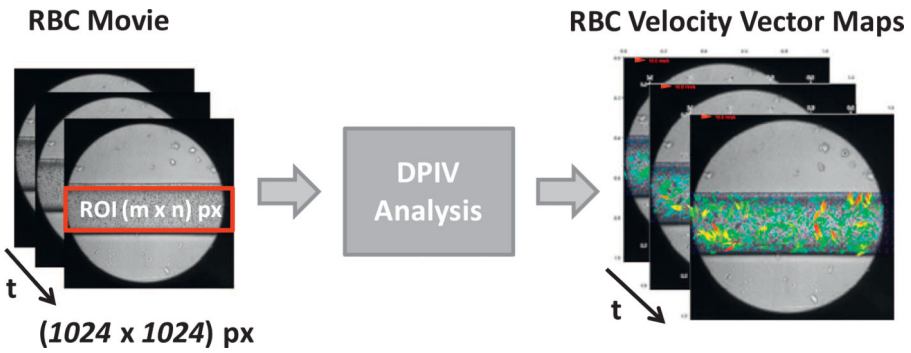


**Fig. 2.**

The DPIV analysis from the RBCs flow movies to the RBCs time-varying velocity vectors maps $V(t)$. In the velocity vectors maps the arrows display the RBCs velocity in directions and magnitudes.

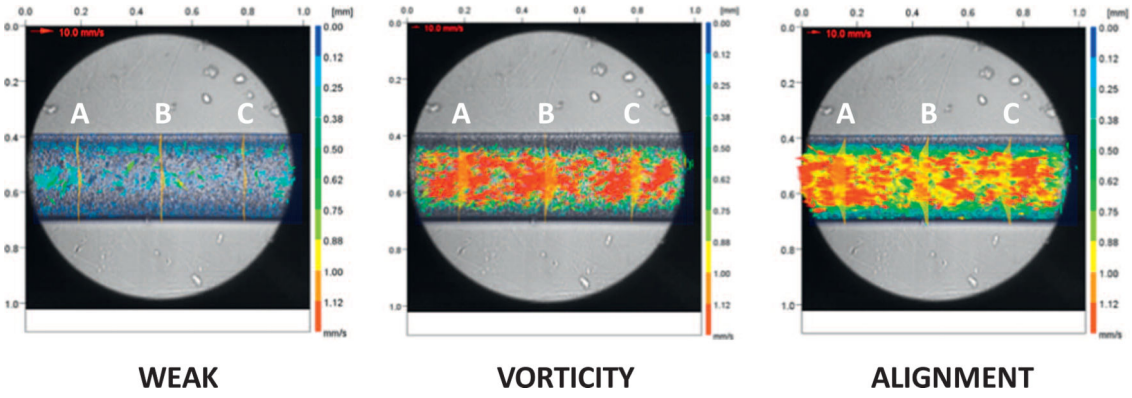


**Fig. 3.**

Examples of the three RBCs flow patterns identified {*Weak Activity*, *Vorticity*, *Alignment*} represented by their velocity vectors maps. The velocity profiles are shown in three microchannel sections {A, B, C}.

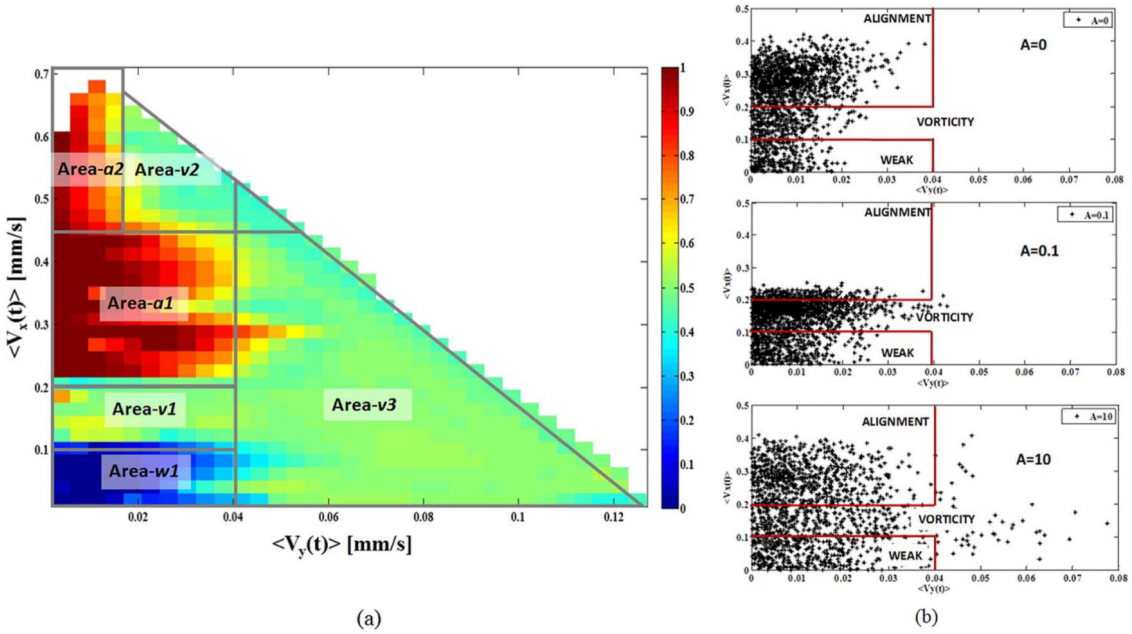


**Fig. 4.**

(a) The map that establishes the relation between the RBCs flow patterns and the RBCs velocities along the horizontal ($|\langle V_x(t)\rangle|$) and vertical ($|\langle V_y(t)\rangle|$). The x-axis and the y-axis report respectively the $|\langle V_y(t)\rangle|$ and the $|\langle V_x(t)\rangle|$ values in [mm/s], whereas the color codes the behaviors: “0” for the *Weak Activity*, “0.5” for the *Vorticity* and “1” for the *Alignment*. (b) The three scattering plots related to ($|\langle V_y(t)\rangle|$, $|\langle V_x(t)\rangle|$) for the experiments $A \in \{0; 0.1; 10\}$. All these experiments reach the *Alignment*.

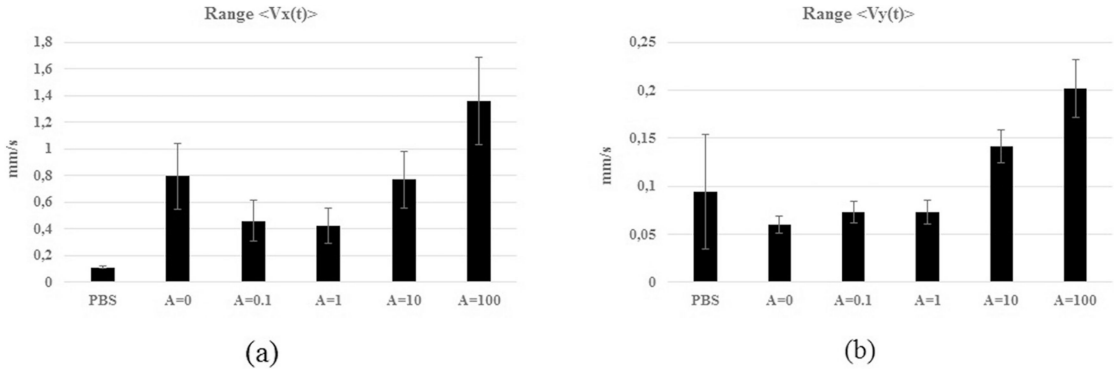


**Fig. 5.**

Histograms of the range of variation and standard deviation of the signals (a) $\langle V_x(t) \rangle$ and (b) $\langle V_y(t) \rangle$ in the six experiments.

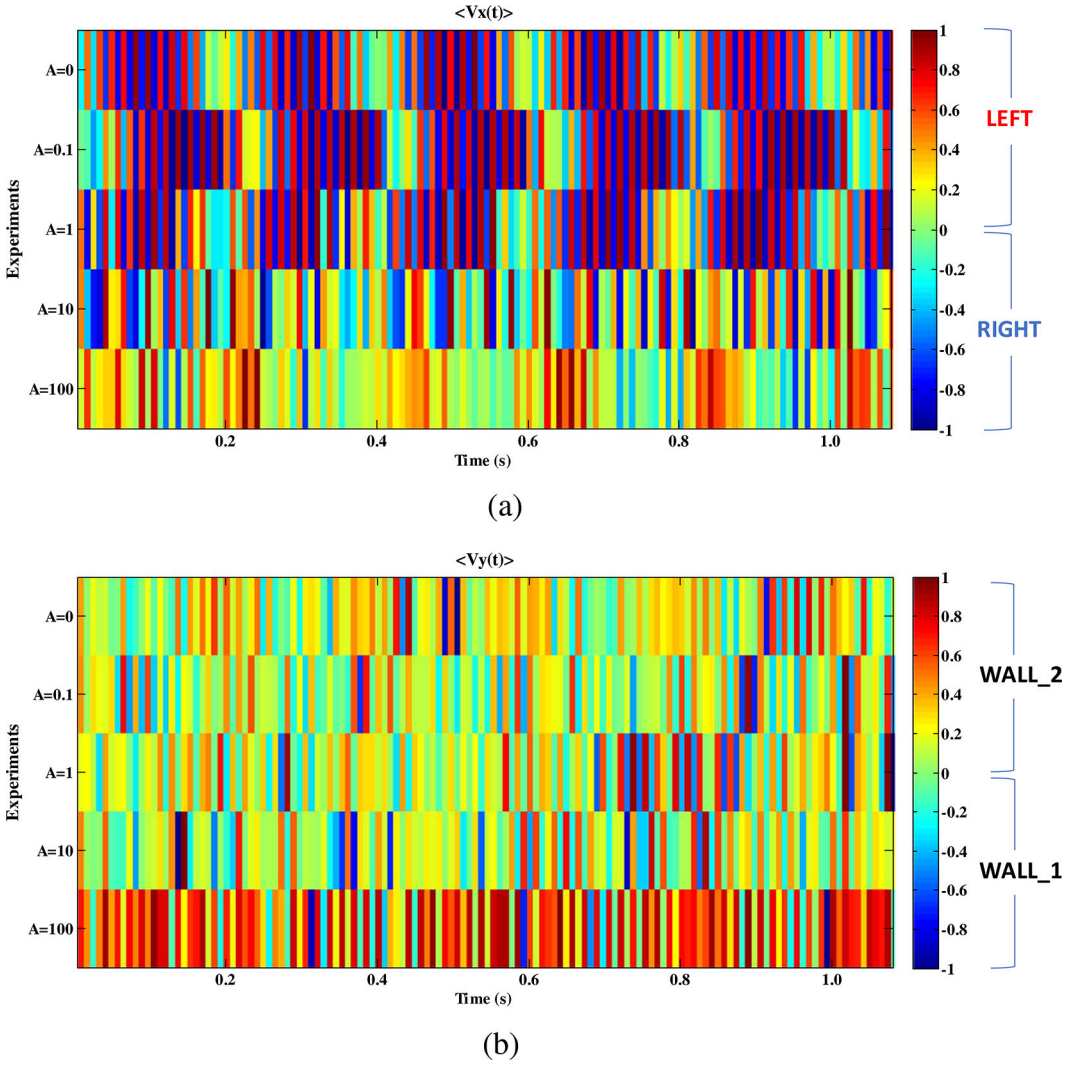


**Fig. 6.**

The velocities signals ($\langle V_x(t)\rangle$, $\langle V_y(t)\rangle$) for all the five experiments $A \in \{0; 0.1; 1; 10; 100\}$ obtained by a spatial averaging the relative matrices ($\langle V_x(t)\rangle$, $\langle V_y(t)\rangle$) and plotted using a color-coded representation in a time window of 1 s. The signals ($\langle V_x(t)\rangle$, $\langle V_y(t)\rangle$) were normalized in the range [−1; 1]. (a) Comparison of $\langle V_x(t)\rangle$ trends: particles displacements toward the left direction for positive values (red arrow) and the right direction for negative values (blue arrow). (b) Comparison of $\langle V_y(t)\rangle$ trends: the positive values are for movements toward the wall_2 (down), and the negative for movements toward the wall_1 (up). (For interpretation of the references to color in this figure legend, the reader is referred to the web version of this article.)

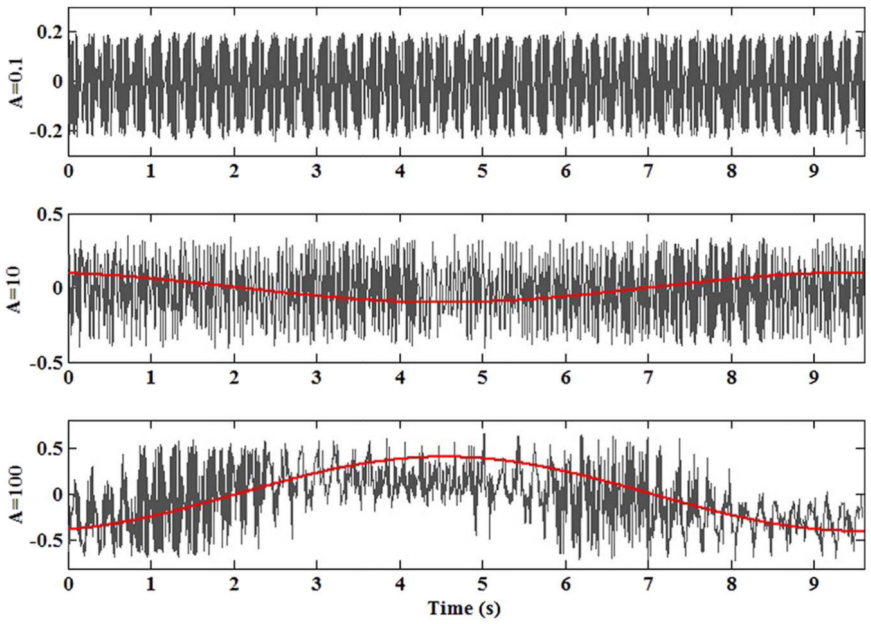


**Fig. 7.**

The trends of velocity along the horizontal axis $\langle V_x(t) \rangle$ for the experiments $A \in \{0.1; 10; 100\}$ in a time interval of 10 s. The red line reproduces the trend of the periodic pressure wave at $f = 0.1$ Hz detected for $A \in \{10; 100\}$. (For interpretation of the references to color in this figure legend, the reader is referred to the web version of this article.)

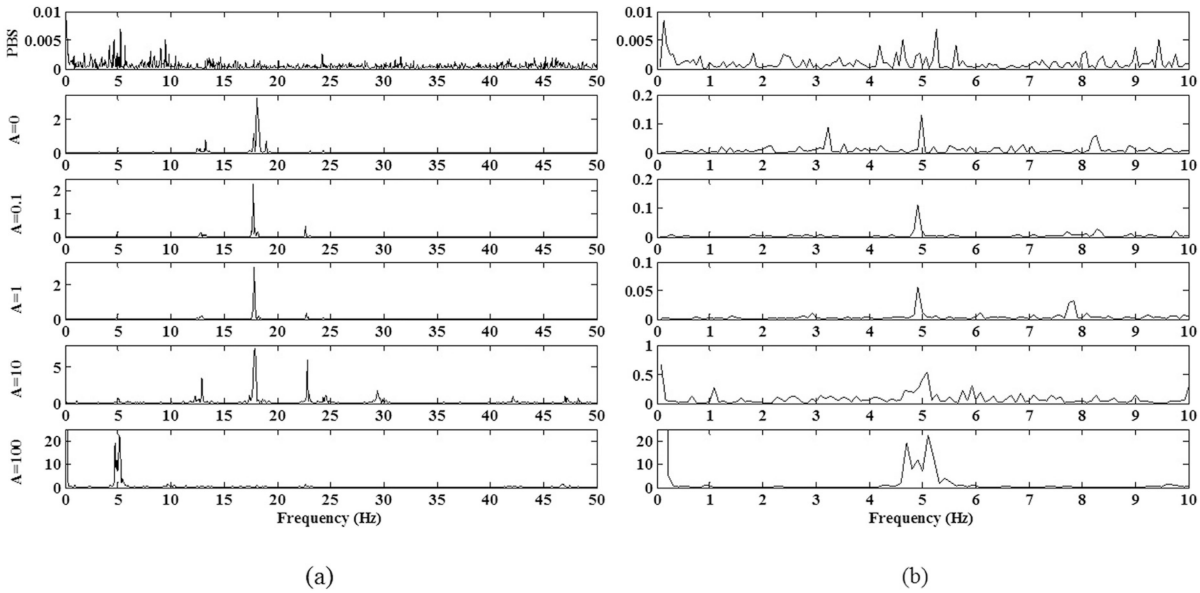


**Fig. 8.**

The spectra of $\langle V_x(t) \rangle$ (a) for the PBS flow and the five experimental conditions $A \in \{0; 0.1; 1; 10; 100\}$. The frequencies components at $f \in \{5; 17.5\}$ Hz have been selected as the most significant being highly sensitive to the experimental conditions and at the same time dominant at least in one experiment. They correspond to the time periods respectively $T \in \{0.2; 0.06\}$ s. (b) A zoom of the spectra in the range $f \in [0.08; 10]$ Hz.

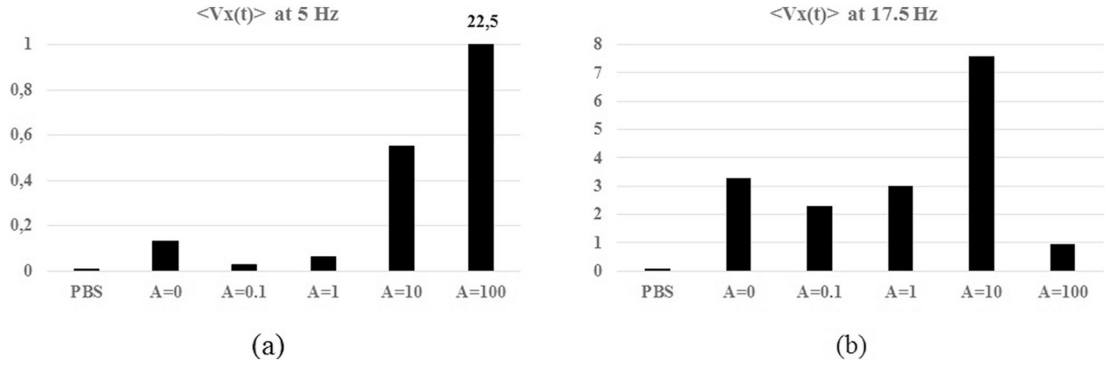


**Fig. 9.**

Histograms of the amplitude of the peaks in the $\langle V_x(t) \rangle$ spectra per experiment (a) $f = 5$ Hz; (b) $f = 17.5$ Hz.

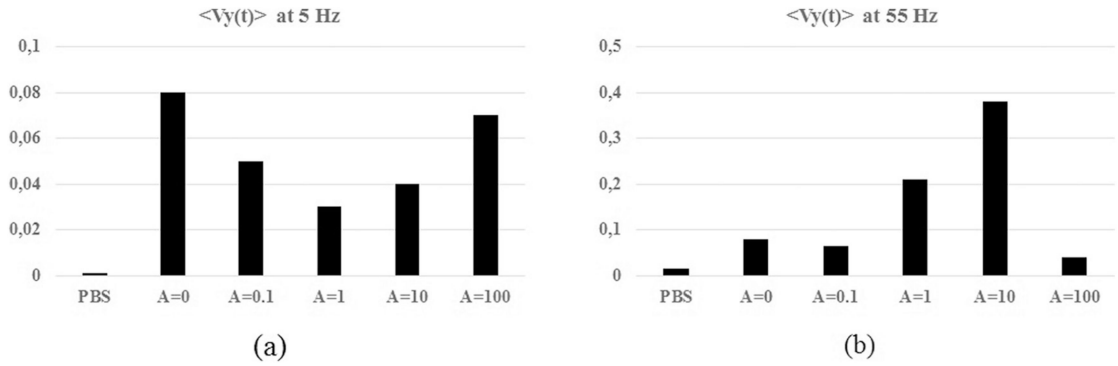


**Fig. 10.**

Histograms of the amplitude of the peaks in the $\langle V_y(t) \rangle$ spectra per experiment (a) $f = 5$ Hz; (b) $f = 55$ Hz.

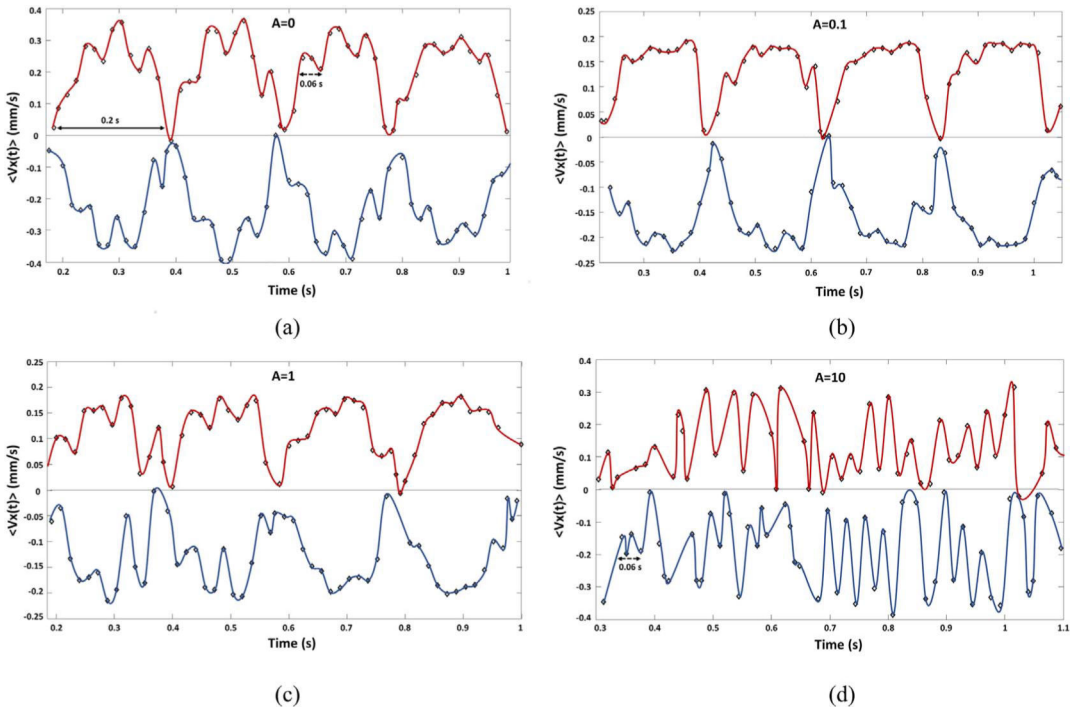


**Fig. 11.**

The signals ($\langle V_{xL} \rangle$, $\langle V_{xR} \rangle$) are plotted respectively in red and blue lines in a time window including two periods of 0.2 s. The arrows evidence the significant periods: solid arrow T = 0.2 s, dotted arrow T = 0.06 s. (a) $A = \{0\}$. (b) $A = \{0.1\}$. (c) $A = \{1\}$. (d) $A = \{10\}$. (For interpretation of the references to color in this figure legend, the reader is referred to the web version of this article.)

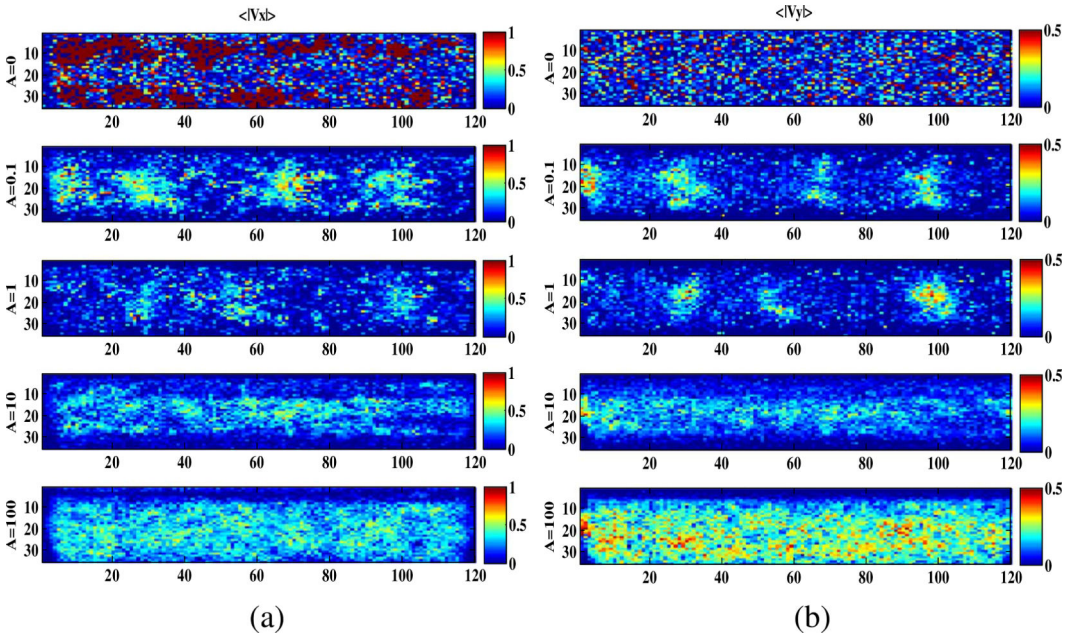


**Fig. 12.**

The spatial velocity maps obtained by the temporal average of the velocity matrices $V_x(t)$ and $V_y(t)$ per $A \in \{0, 0.1; 1; 10; 100\}$. The right column (a) is for $|\langle V_x \rangle|$ and the left column (b) is for $|\langle V_y \rangle|$. A color-coded threshold was used.

**Table 1**

Statistics on the signals $\langle V_x(t) \rangle$ and $\langle V_y(t) \rangle$ : the range of variation and standard deviation in [mm/s].

| | | **PBS** | ***A* = 0** | ***A* = 0.1** | ***A* = 1** | ***A* = 10** | ***A* = 100** |
|---|---|---|---|---|---|---|---|
| $\langle V_x(t) \rangle$ | Range | 0.011 | 0.796 | 0.459 | 0.424 | 0.768 | 1.358 |
| | Std | 0.007 | 0.047 | 0.155 | 0.133 | 0.214 | 0.331 |
| $\langle V_y(t) \rangle$ | Range | 0.094 | 0.06 | 0.073 | 0.073 | 0.141 | 0.202 |
| | Std | 0.006 | 0.009 | 0.011 | 0.012 | 0.017 | 0.03 |